

Pull-out behaviour of two post-grouted anchors: fibre-optic strain measurements and numerical simulations

Comportement de deux tirants d'ancrage injectés: instrumentation à fibres optiques et simulations numériques

C. Fabris

Graz University of Technology, Graz, Austria

H. F. Schweiger, H. Woschitz

Graz University of Technology, Graz, Austria

V. Račanský

Keller Grundbau, Vienna, Austria

ABSTRACT: This paper presents the results of two pull-out tests of ground anchors. The anchors were post-grouted and one anchor was additionally monitored with a fibre-optic sensing system. The fibres were installed along the steel tendon and along the grout. Due to difficulties encountered during the post-grouting of one anchor, the anchors showed distinctly different load-displacement behaviour. In-situ and laboratory investigations were performed and numerical simulations were carried out. The numerical model was able to capture the load-displacement behaviour of the anchors and the strain profile along the tendon was well reproduced by the numerical simulation. The distribution of cracks in the grout obtained with the numerical simulation compared well with the in-situ measurements.

RÉSUMÉ: Dans cet article, sont présentés les résultats de deux essais d'arrachement d'ancrages de terrain. Le coulis a été injecté sous pression et un ancrage a été surveillé en utilisant des fibres optiques. Les fibres optiques ont été installées sur la longueur des barres de l'ancrage et dans le coulis de ciment. En raison de difficultés lors de l'injection du coulis d'un ancrage, les essais ont indiqué des comportements différents. Des investigations in situ et en laboratoire ont été effectuées, ainsi que des calculs numériques. Le modèle numérique a été capable de simuler le comportement charge-déplacement des ancrages et de reproduire les déformations des barres d'acier. Le modèle adopté pour simuler le coulis de ciment a bien capturé la distribution des fissures dans le ciment et les capacités du modèle numérique ont été vérifiées.

Keywords: post-grouted anchors; numerical simulations; fibre-optic measurements

1 INTRODUCTION

In order to evaluate the load transfer mechanism of ground anchors, two load tests were performed on post-grouted anchors and the displacements were monitored with a linear transducer. Additionally, one anchor was monitored with a distributed fibre-optic sensing system and the fibres

were installed along the steel strands and along the grout.

Distributed fibre-optic sensing systems enable a continuous and accurate measurement of strains, with a spatial resolution of less than 10 mm. Although such monitoring systems have

gained attention in recent years, strain measurements during load tests of geotechnical structures are traditionally performed using local sensors such as strain gauges.

A class-A numerical prediction was performed prior to the anchors pull-out tests and compared with the in-situ results. The parameters required for the numerical simulation were calibrated with laboratory and in-situ tests. After the in-situ pull-out tests, new laboratory tests were carried out on soil and grout samples and the numerical prediction was refined.

2 DESCRIPTION OF THE PULL-OUT TESTS

The anchors were installed in October 2017 and were post-grouted at the fixed length in the following day. The pull-out tests were performed six weeks after the anchors were installed. The soil is a clayey silt, locally known as “Seeton”, and consists of approximately 60-70 % silt, 15-30 % clay and 10-15 % sand. Silty sand layers were identified during a core drilling performed close to the location of the pull-out tests and the particle size distribution was approximately 5 % gravel, 50 % sand, 40 % silt and 5% clay.

Both anchors were installed vertically and were 12 m long at the free length and 8 m long at the fixed length. Six strands were employed (high-grade steel Y1860, 6 x 15.7 mm) and the borehole diameter was 178 mm.

A linear transducer was installed at the anchor head to measure the displacements during the pull-out test. Additionally, one anchor was monitored with a distributed fibre-optic system along the tendon and along the grout. The anchor monitored with the linear transducer and with the fibre-optic system is referred as anchor 1A and the anchor monitored only with the linear transducer is referred as anchor 1B.

Although both anchors were designed to have the same geometry, due to problems encountered during the post-grouting of the anchor 1B the

planned volume of cement could not be fully injected. The diameter of the grouted body along the fixed length was back-calculated according to the volume of cement and is shown in Table 1. The anchors geometry is presented in Figure 1.

Table 1. Grout diameter along the fixed length

Anchor	Volume of cement (l)	Diameter (m)
1A	300	0.28
1B	184	0.25

Two strands were monitored during the pull-out test of anchor 1A and the fibres were glued following the torsion of the wires, which protects the sensing cable well. The grout was instrumented with more robust cable types, which were attached outside the corrugated pipe using adhesive tape.

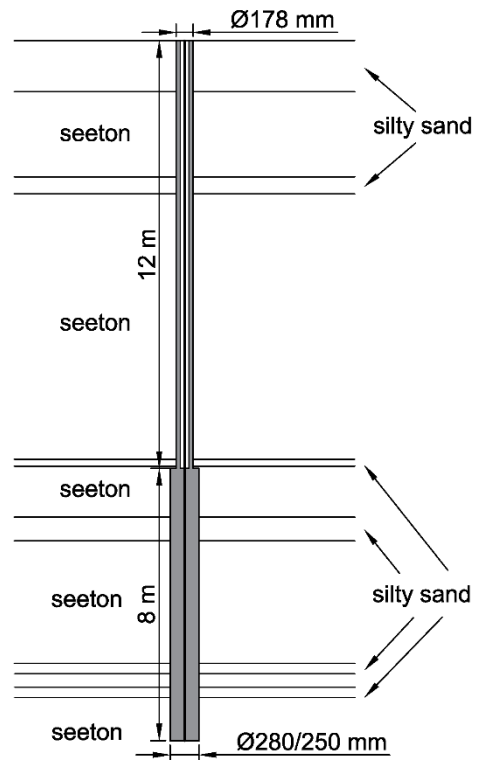


Figure 1. Anchor geometry

3 NUMERICAL SIMULATIONS

Prior to the anchors pull-out tests, a class-A prediction was performed and the soil parameters were adopted according to laboratory and in-situ investigations. Further laboratory tests were carried out on grout and soil samples after the anchors pull-out tests and consequently the numerical simulation was refined.

3.1 Constitutive models

The soil was modelled with the Hardening soil model with small-strain stiffness (HS_{small} model), an elasto-plastic constitutive model which considers shear hardening and compression hardening by implementing a cone yield surface and a cap yield surface (Schanz *et al.*, 1999). The high stiffness at small-strain levels is also taken into account (Benz, 2007). The secant stiffness for deviatoric loading ($E_{50,ref}$), the tangent stiffness for oedometer loading ($E_{oed,ref}$), the unloading/reloading stiffness ($E_{ur,ref}$), and the small-strain shear modulus ($G_{0,ref}$) are input parameters and are related to a reference pressure, taken in this study as 100 kPa. Moreover, the threshold shear strain ($\gamma_{0.7}$), at which the secant shear modulus is reduced to about 70 % of the small-strain shear modulus, is implemented.

The Concrete model was the constitutive model employed for the grout. The model is capable of considering the time-dependent strength and stiffness development, strain hardening and softening, creep, and shrinkage. As the primary grouting and the post-grouting of the anchors were performed several weeks before the pull-out test, no time-dependency is taken into account. In tension, the model behaviour is linear elastic until the tensile strength ($f_{t,28}$) is achieved. Linear strain softening follows until a residual strength is reached. Softening in tension is governed by the input parameter $G_{t,28}$, which is the fracture energy in tension. A regularisation technique is implemented to avoid mesh dependency due to softening. For more details on the model, the reader is referred to Schädlich & Schweiger (2014) and Brinkgreve *et al.* (2018).

3.2 Class-A prediction

The description of the laboratory and in-situ tests for the Seeton is presented below. Strength parameters obtained from direct shear tests led to a friction angle of 29.5° and a cohesion intercept of 10 kPa. Oedometer tests were carried out and numerically calibrated. The reference oedometer stiffness was 5300 kPa and the reference secant stiffness was adopted as $E_{50,ref} = 1.25E_{oed,ref}$.

An in-situ seismic dilatometer test (sDMT) was performed and the shear wave velocity profile (V_s) is presented in Figure 2. The small-strain shear modulus (G_0) was then calculated according to Equation 1.

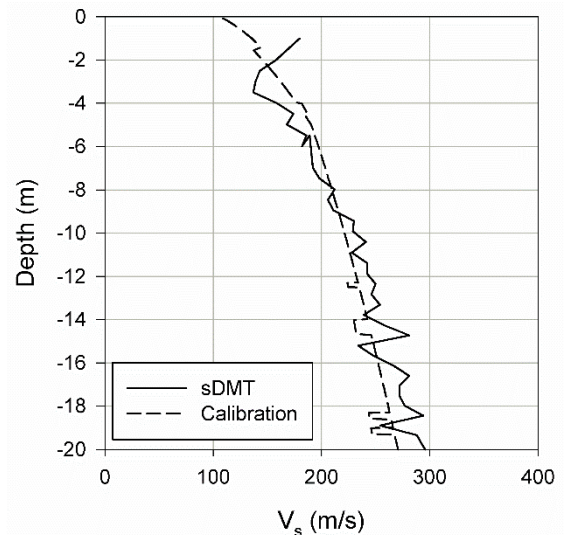


Figure 2. Calibration of the shear wave velocity

$$G_0 = \rho \cdot V_s^2 \quad (1)$$

Where ρ is the material density (kg/m^3) and V_s is the shear wave velocity (m/s). Based on experience from analyses on similar ground conditions, the unloading/reloading shear modulus was assumed as $G_{ur,ref} = G_{0,ref}/6$ and $E_{ur,ref}$ was then back calculated, leading to $E_{ur,ref} \approx 9E_{oed,ref}$.

The silty sand layers identified during the core drilling were also observed with the sDMT, as indicated by the material index I_D (Figure 3). One can notice that I_D values obtained for the Seeton

suggest a clayey material and not a silty material, although the grain size distribution indicates about 60-70 % silt. The small values of I_D observed during the test can be explained by partial drainage of the Seeton, leading to a misinterpretation of the material index. The position of the silty sand layers considered in the numerical model was based on the I_D profile.

The main parameters adopted for the class-A prediction are shown in Table 2 and Table 3. The values assumed for the silty sand layers and for the grout were not numerically calibrated but were based on investigations performed on similar materials. In Table 3, E_{28} is the Young's modulus, $f_{c,28}$ and $f_{t,28}$ are the uniaxial compressive and tensile strength, $G_{c,28}$ and $G_{t,28}$ are the compressive and tensile fracture energies and ϕ_{\max} is the friction angle. The tendon was simulated as a linear elastic material and the adopted Young's modulus was 195 GPa.

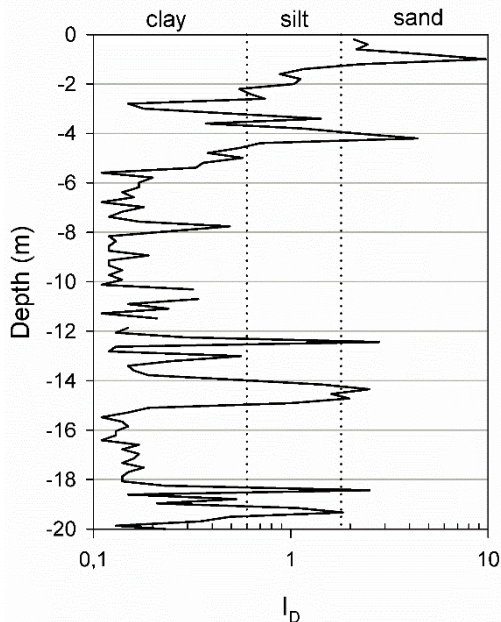


Figure 3. Material index from the sDMT

Table 2: Soil parameters (HSsmall model)

Parameter	Seeton Value	Silty Sand Value
$E_{50,ref}$ (kPa)	6625	24000

$E_{oed,ref}$ (kPa)	5300	24000
$E_{ur,ref}$ (kPa)	48000	48000
c'_{ref} (kPa)	10	5
ϕ' ($^{\circ}$)	29.5	35
m	0.9	0.6
v'_{ur}	0.2	0.2
$G_{0,ref}$ (kPa)	120 000	120 000
$\gamma_{0.7}$	0.15E-3	0.15E-3

Table 3: Grout parameters (Concrete model)

Parameter	Grout Value
E_{28} (GPa)	16.3
$f_{c,28}$ (MPa)	32.1
$f_{t,28}$ (MPa)	2
$G_{c,28}$ (kN/m)	50
$G_{t,28}$ (kN/m)	0.15
ϕ_{\max} ($^{\circ}$)	40

3.3 Numerical refinement

During grouting, cement probes with a water-cement ratio of approximately 0.6 were prepared for laboratory investigations on the grout and the samples were tested after about 28 days of curing time. Displacement controlled uniaxial compressive tests and multistage triaxial tests were calibrated for the pre-peak regime.

Two indirect splitting tensile tests were performed. The measured grout tensile strength was 1.0 MPa and 1.2 MPa. Because the Concrete model requires the uniaxial tensile strength obtained from direct uniaxial tensile test ($f_{t,28}$), this parameter was increased to 1.5 MPa based on correlations between direct and indirect tensile strength (Berenbaum & Brodie, 1959; Lin & Wood, 2003).

Schweiger *et al.* (2014) suggest values for $G_{t,28}$ between 0.01 to 0.05 kN/m for jet grout material. The fracture energy in tension of 0.01 kN/m was adopted herein and, after numerical evaluation of the crack development along the grout and comparison with the fibre-optic measurements, this value seemed to be reasonable. The fracture energy in compression ($G_{c,28}$) was adopted equal to 3 kN/m. However, because the grout at the fixed

length is subjected mainly to tensile stresses, $G_{c,28}$ has little effect on the results in this particular case.

Additionally, an oedometer laboratory test was carried out on a silty sand sample and the stiffness parameters of this material were modified. The parameters modified after numerical refinement are shown in Table 4.

Table 4: Modified parameters

Parameter	Previous	Modified	Material
$E_{50,ref}$ (kPa)	24000	16000	Sand
$E_{oed,ref}$ (kPa)	24000	16000	
$E_{ur,ref}$ (kPa)	72000	48000	
E_{28} (GPa)	16.3	15.5	Grout
$f_{c,28}$ (MPa)	32.1	30.6	
$f_{t,28}$ (MPa)	2	1.5	
$G_{c,28}$ (kN/m)	50	3	
$G_{t,28}$ (kN/m)	0.15	0.01	
ϕ_{max} (°)	40	48	Tendon
E (GPa)	195	160	

3.4 Model geometry

The geometry employed in the numerical simulations is shown in Figure 4. The model was axisymmetric and the load was applied by means of vertical prescribed displacements at the top of the fixed length. For this reason, the load at the free length is assumed to be fully transferred to the fixed length. The grout is considered along the free length, for corrosion protection, and along the fixed length.

In the class-A prediction, no distinction was made between anchors 1A and 1B. The post-grouting was considered by increasing the diameter along the fixed length to 280 mm and the coefficient of lateral earth pressure (K_0) was set as 1 instead of $1 - \sin\phi'$. For the numerical refinement of anchor 1B, the diameter at the fixed length and K_0 were decreased to 250 mm and 0.6, respectively, in order to account for a “partial” post-grouting effect.

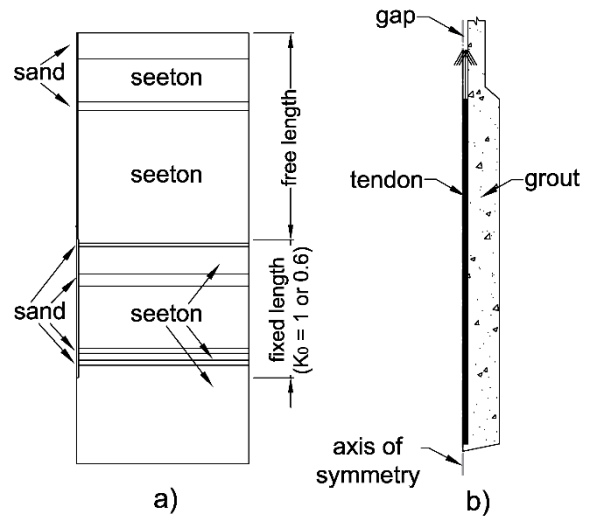


Figure 4. Model geometry – a) soil layers and b) detail of the fixed length

4 IN-SITU RESULTS

In Figure 5 the measured load-displacement curves are presented. Only the displacements at the top of the fixed length are shown, *i.e.* the elastic elongation of the free length was subtracted from the total displacement measured at the anchor head. The dashed lines indicate the load stage at which the creep rate exceeded 2 mm, which is the usually adopted failure criteria of in-situ tests. Anchor 1A, which was successfully post-grouted, showed higher ultimate load and stiffer behaviour than anchor 1B.

Post-grouting results in an increase in radial stresses along the grout-soil interface. Ostermayer (1975) presented results of a large number of tests and showed that the post-grouting technique increased the skin friction in stiff clay of medium to high plasticity from about 120 kN/m² up to 300 kN/m², whereas in very stiff clays the increase ranged from 25% to 50%.

The fibre-optic strain measurements along the tendon are shown in Figure 6 for several load stages. The free length is located within the first 12 m and the fixed length within the last 8 m. Negative values denote compressive strains and positive values tensile strains.

Due to the fact that the strands were encapsulated at the free length, no load from the tendon to the grout was transferred in the first 12 m and the strains were essentially constant. At the beginning of the fixed length the strains started to decrease and at 1100 kN almost the entire tendon was activated.

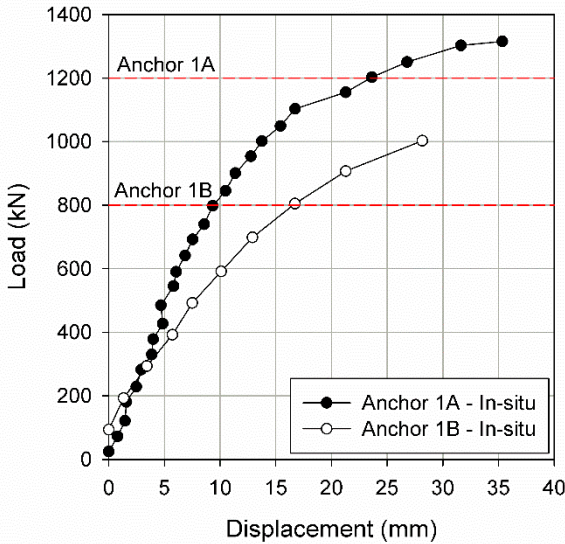


Figure 5: In-situ load-displacement curves

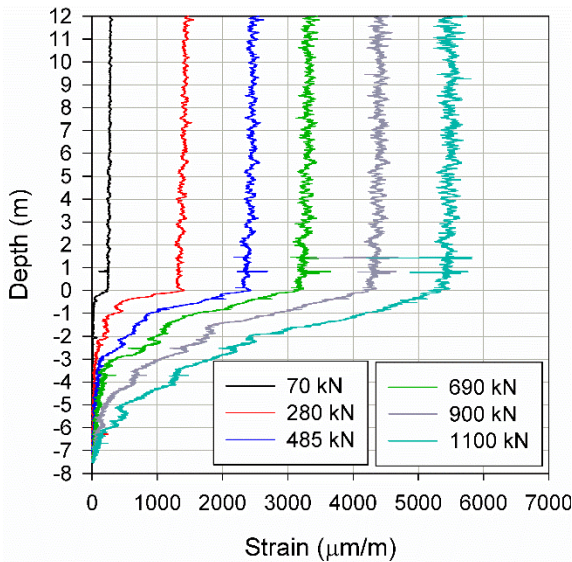


Figure 6. Fibre-optic measurements along the tendon

Regarding the grout measurements, the strains are presented in Figure 7. The grout at the free length was subjected to compression and at the fixed length negative strains became positive, indicating tensile stresses. The peaks observed along the grout suggest that cracking evolves during the pull-out test.

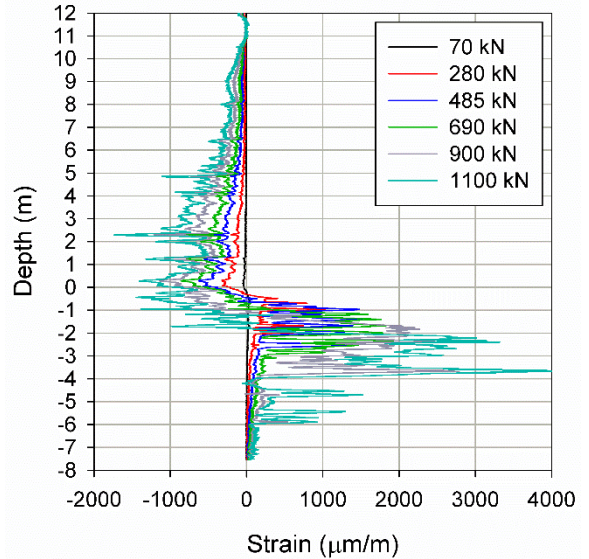


Figure 7. Fibre-optic measurements along the grout

5 COMPARISON IN-SITU AND NUMERICAL RESULTS

The measured load-displacement curves and the numerical results are shown in Figure 8 and Figure 9. The horizontal bars show the anchor displacements if the measured creep is subtracted from the final displacement.

The predicted load-displacement curve showed very good agreement with the measured curve. The numerically predicted ultimate load was 1100 kN and anchor 1A achieved the failure criteria at 1200 kN during the pull-out test. After numerical refinement, in-situ and numerical curves led to the same ultimate load. Predicted and refined curves showed slightly stiffer behaviour than the measured curve, but if the creep is subtracted from the displacement, the differences

between measurements and both numerical results were not significant from a practical point of view.

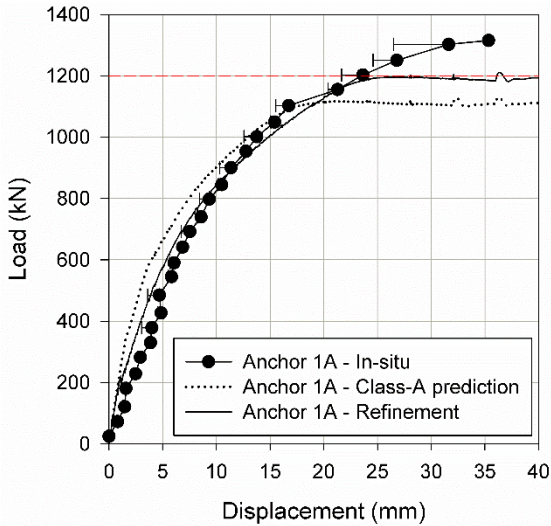


Figure 8. In-situ and numerical load-displacement curves (anchor 1A)

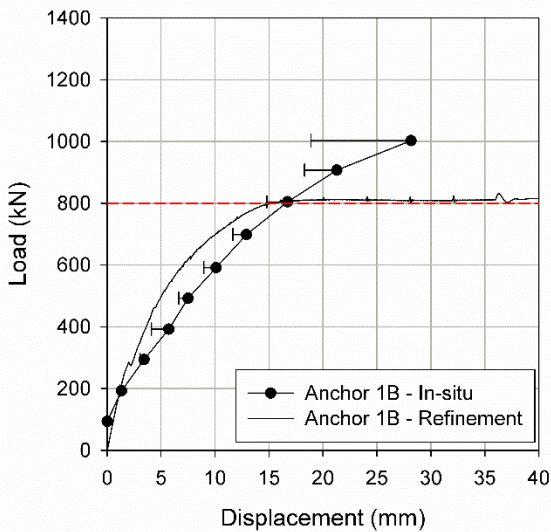


Figure 9. In-situ and numerical load-displacement curves (anchor 1B)

Regarding anchor 1B, after the diameter of the grout along the fixed length was decreased and K_0 was set as 0.6, the simulated curve achieved the same ultimate load as the measured one, if the “creep-criterion” is accepted for defining failure.

As observed for anchor 1A, the simulated load-displacement curve showed stiffer behaviour than the in-situ curve.

The comparison between the fibre-optic strain measurements along the tendon and the numerical results is shown in Figure 10. Only the strains along the fixed length are presented.

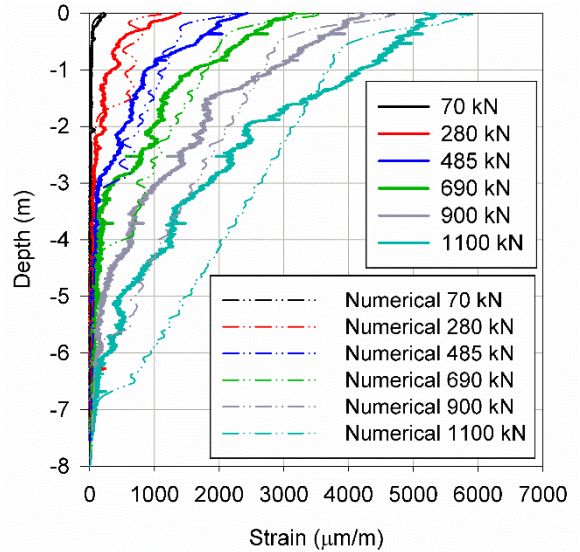


Figure 10. Measured and numerical strains along the tendon (fixed length)

The numerical oscillations in Figure 10 are the result of snap-back instability generated when cracking in the grout starts. As soon as cracking starts, softening takes place within the crack and the zone around it unloads elastically. If the unloading energy is greater than the energy dissipated by the crack, both forces and displacements must decrease to reach equilibrium (Carpinteri & Colombo, 1989; Brinkgreve *et al.*, 2018). Since the numerical simulation is displacement-controlled, the applied displacement cannot decrease and the force drops vertically at constant displacement in the load-displacement diagram.

The monitored strains along the grout are compared in Figure 11 with the tension softening parameter (H_t), an output of the Concrete model. Values of H_t greater than zero implies that cracking has started and values greater than 1 indicates

residual state. The Concrete model was able to reproduce crack development and at the load stage of 1100 kN cracking is observed along almost the entire fixed length.

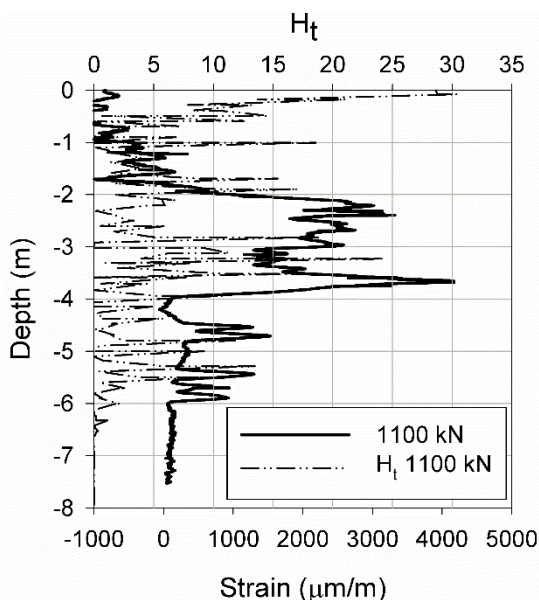


Figure 11. Measured and numerical crack development along the grout (fixed length)

6 CONCLUSIONS

Two ground anchor pull-out tests were performed in Austria, namely anchors 1A and 1B. The anchors were post-grouted and anchor 1A was monitored with a fibre-optic sensing system. A class-A numerical prediction was performed and compared with the in-situ results. Moreover, after additional soil and grout laboratory investigations, the numerical model was improved and the results were compared with the measurements.

The predicted load-displacement curve compared very well with the in-situ measurement of anchor 1A. Regarding anchor 1B, the geometry of the grouted body and the coefficient of lateral earth pressure were decreased to account for the “partial” post-grouting effect. The strains along the tendon showed good agreement with the fibre-optic measurements and the distribution of cracks was well reproduced.

7 ACKNOWLEDGEMENTS

The results presented herein have been developed within the framework of the FFG-Project (Bridge-24 No. 858505) with the support of ÖBB Infrastruktur and Asfinag.

8 REFERENCES

- Benz, T. 2007. *Small-Strain Stiffness of Soils and its Numerical Consequences*: PhD thesis, Universität Stuttgart, Stuttgart.
- Berenbaum, R., Brodie, I. 1959. Measurement of the tensile strength of brittle materials. *British Journal of Applied Physics* **10**, 281-287.
- Brinkgreve, R. B. J., Kumarswamy, S., Swolfs, W. M., Foria, F. 2018. *Plaxis 2D Material Models Manual*. Delft: Plaxis bv.
- Carpinteri, A., Colombo, G. 1989. Numerical analysis of catastrophic softening behaviour (snap-back instability), *Computers and Structures* **31**, No. 4, 607-636.
- Lin, Z., Wood, L. 2003. Concrete uniaxial tensile strength and cylinder splitting test. *Journal of Structural Engineering* **129**, 692-698.
- Ostermayer, H. 1975. Construction, carrying behaviour and creep characteristics of ground anchors. *Proceedings, Conference on Diaphragm Walls and Anchorages*, 141-151.
- Schädlich, B., Schweiger, H.F. 2014. A new constitutive model for shotcrete. *Proceedings, 8th European Conference on Numerical Methods in Geotechnical Engineering*, 103-108.
- Schanz, T.; Vermeer, P.A.; Bonnier, P.G. 1999. The hardening soil model: formulation and verification, *Beyond 2000 in Computational Geotechnics*, 281-290.
- Schweiger, H. F., Sedighi, P., Henke, S., Borchert, K.-M. 2014. Numerical modelling of ground improvement techniques considering tension softening. *Proceedings, 8th International Symposium on Geotechnical Aspects of Underground Construction in Soft Ground*, 209-214.